

A high-performance watermelon skin ion-solvating membrane for electrochemical CO₂ reduction

Received: 11 January 2024

Accepted: 31 July 2024

Published online: 07 August 2024



Qinglu Liu^{1,2,3,4,7}, Tang Tang^{1,2,3,4,7}, Ziyu Tian^{1,2,3,4}, Shiwen Ding^{1,2,3,4},
Linqin Wang^{1,2,3,4}, Dexin Chen^{1,2,3,4}, Zhiwei Wang^{1,2,3,4}, Wentao Zheng^{1,2,3,4},
Husileng Lee^{1,2,3,4}, Xingyu Lu⁵, Xiaohe Miao⁶, Lin Liu⁶ & Licheng Sun^{1,2,3,4} ✉

Ion-solvating membranes have been gaining increasing attention as core components of electrochemical energy conversion and storage devices. However, the development of ion-solvating membranes with low ion resistance and high ion selectivity still poses challenges. In order to propose an effective strategy for high-performance ion-solvating membranes, this study conducted a comprehensive investigation on watermelon skin membranes through a combination of experimental research and molecular dynamics simulation. The micropores and continuous hydrogen-bonding networks constructed by the synergistic effect of cellulose fiber and pectin enable the hypodermis of watermelon skin membranes to have a high ion conductivity of 282.3 mS cm⁻¹ (room temperature, saturated with 1 M KOH). The negatively charged groups and hydroxyl groups on the microporous channels increase the formate penetration resistance of watermelon skin membranes in contrast to commercially available membranes, and this is crucial for CO₂ electro-reduction. Therefore, the confinement of proton donors and negatively charged groups within three-dimensional microporous polymers gives inspiration for the design of high-performance ion-solvating membranes.

Ion-transport membranes (ITMs) are key components in many state-of-the-art renewable energy conversion systems, such as electrochemical carbon dioxide reduction reaction (CO₂RR)^{1,2}, water splitting^{3–5}, and fuel cells^{6,7}. In the electrochemical process of these technologies, ions are transported between two half-cells through ITMs. The efficacy of ITMs depends on their ability to transport ions rapidly and selectively^{8–10}.

Currently, the widely used ITMs can be divided into four categories: porous diaphragms¹¹, proton exchange membranes (PEMs)¹², anion exchange membranes (AEMs)^{8,13} and ion-solvating membranes (ISMs)^{14,15}. Among them, porous diaphragms are mainly used in alkaline

electrolyzers, but they commonly have issues with high resistance and poor gas-blocking properties. PEMs are suitable for acidic systems which makes PEM electrolyzers expensive and rely on expensive platinum group electrocatalysts. To reduce the dependence on platinum group electrocatalysts, researchers are developing AEMs for alkaline environments as an alternative¹³. The AEM always contains cationic functional groups in the polymer chain, which enables the transport of anions through a surface site hopping mechanism. However, the ion conductivity of AEMs is still lower than that of PEMs due to the larger size of OH⁻^{16,17} and the weak basicity of the cation site¹⁸. The common

¹Center of Artificial Photosynthesis for Solar Fuels and Department of Chemistry, Westlake University, 600 Dunyu Road, Hangzhou 310030 Zhejiang Province, China. ²School of Science and Research Center for Industries of the Future, Westlake University, 600 Dunyu Road, Hangzhou 310030 Zhejiang Province, China. ³Institute of Natural Sciences, Westlake Institute for Advanced Study, 18 Shilongshan Road, Hangzhou 310024 Zhejiang Province, China. ⁴Division of Solar Energy Conversion and Catalysis at Westlake University, Zhejiang Baima Lake Laboratory Co., Ltd, Hangzhou 310000 Zhejiang Province, China.

⁵Instrumentation and Service Center for Molecular Science, Westlake University, Hangzhou 310024, China. ⁶Instrumentation and Service Center for Physical Sciences, Westlake University, Hangzhou 310024, China. ⁷These authors contributed equally: Qinglu Liu, Tang Tang. ✉e-mail: sunlicheng@westlake.edu.cn

method to prepare high-anion-conductivity membranes is to increase the ion exchange capacity, but this method often compromises the mechanical strength¹⁹. Some other methods such as hydrophobicity engineering^{20,21} and ultramicroporous structure design^{7,22} also improved the ion conductivity by modifying the molecular structure. However, the stability of such structures still relies on the structure of the cationic functional group. Currently, the most commonly used cationic functional group is the ammonium salt, which may undergo nucleophilic attack under alkaline conditions, leading to degradation through nucleophilic substitution reaction or Hofmann elimination, gradually reducing the ion conductivity²³.

In addition, by considering the mechanism of the surface site hopping process (Fig. 1a), when AEMs are utilized in CO₂ electro-reduction devices, not only OH⁻, but also cathode products like HCOO⁻ and CH₃COO⁻ are transported from the cathode to the anode through the membranes. This phenomenon has a detrimental effect on product collection and the objective evaluation of the cathode catalyst's performance. The challenge of achieving selectivity for specific anions through AEMs still remains^{24,25}. Constructing microporous channels in AEMs is an emerging strategy to improve ion conductivity and regulate the ion selectivity^{7,9,26,27}. Microporous polymers have a certain interchain gap size (2–20 Å), which provides a low-hindrance transmission path for ions and makes it possible to achieve size selectivity. However, currently, most microporous polymers have poor chemical stability and low mechanical strength^{28,29}. ISMs employ the absorption of aqueous alkaline electrolytes to facilitate ionic conductivity. These membranes do not necessarily function as intrinsic hydroxide conductors. Due to the absence of ammonium salt cation functional groups, this type of membrane does not facilitate the surface site hopping transfer of negative ion products at the cathode. However, ISMs require a high concentration of KOH electrolyte (>3 M) to achieve ion conductivity comparable to that of AEMs. In strong alkaline environments, the stability of their polymer backbone is not ideal, and the electrolyzers are prone to corrosion¹⁴.

Based on the above reasons, the currently reported ISMs are difficult to simultaneously achieve high ion conductivity and high selectivity for anions. As such, it is crucial to formulate a novel design strategy for the advancement of ISMs in response to the growing demands in the field of energy storage and conversion. Nature often inspires scientific research^{30–33}. For example, inspired by the oxygen evolution complex in plant photosystem II, researchers designed and synthesized efficient artificial water oxidation catalysts³⁴. Due to the accompanying ion transport during photosynthesis, respiration, and transpiration in green plants, we speculate that low-energy-barrier ion-transport channels may exist within plant cell walls. Therefore, the revelation of the crucial structure-activity relationships in natural membranes may provide valuable guidance for optimizing the design and synthesis of more advanced artificial ISMs.

To obtain a large and complete skin membrane containing efficient ion transport channels, a high-water content fruit, watermelon, was selected as a potential candidate. This research utilizes watermelon skin ISM obtained through the freezing-exfoliation method as the experimental subject. Through a series of experimental verifications, micropores and continuous hydrogen-bonding networks were found to be formed within the watermelon skin membrane (WSM) under the synergistic effect of cellulose fiber and pectin (high-water-uptake pectin is uniformly filled in an ordered spatial framework composed of cellulose fibers). The coupling of the micropores and continuous hydrogen-bonding networks can effectively accelerate hydroxide transport via the vehicle mechanism and Grotthuss mechanism, respectively. In addition, the microporous channels with organized hydroxyl group and other negatively charged groups restrict the migration of acid ions (such as formate ions) through the negative charge repulsion and hydrogen bond drag forces (Fig. 1b). Furthermore, the WSM can also prevent the permeation of alcohol substances (such as ethanol and propanol). The selective permeability of the WSM to hydroxide and acid radical ions, as well as its barrier property to alcohol substances, are of great significance for inspiring the design of ion transport membranes in CO₂ electroreduction. Therefore, the confinement of microporous polymers rich in proton donors and negatively charged groups within three-dimensional framework systems is expected to become a design strategy for a new generation of ISMs.

Results

The characterization of WSM

We designed a freezing-exfoliation method to afford a uniform WSM (Fig. 2a, left) containing the cuticle, epidermis and part of the hypodermis³⁵, as confirmed by transmission electron microscopy (TEM) (Fig. 2a, right). This study investigated the functions of the three layers composing the WSM (Fig. 2b). The cuticle layer impedes the ion transport of the WSM. The epidermal layer, with high pectin content and closely woven cellulose³⁶, exhibits excellent ion selectivity and mechanical properties. The hypodermis layer showcases remarkable ion transport performance. These specific experimental details are elaborated on later.

The optical microscopic and scanning electron microscopy (SEM) images showcase the overall morphology of the WSM (Fig. 2c–e), which is $75 \pm 5 \mu\text{m}$ thick and composed of well-assembled cell layers. The WSM was characterized using Fourier transform infrared spectroscopy (FTIR)³⁷ and solid-state nuclear magnetic resonance (NMR)³⁸. The characteristic peaks of these two spectra (Fig. 2f and Fig. 2g) indicate that the main components of WSM included cellulose/hemicellulose and pectin³⁹. From Fig. 2f, compared to WSM, the two peaks (2920 cm^{-1} and 2846 cm^{-1}) belong to the -CH₂ antisymmetric and symmetric stretching vibrations respectively, originating from the lipid materials with long alkane chains that constitute the cuticle layer (Fig. S1a, b)^{40,41}.

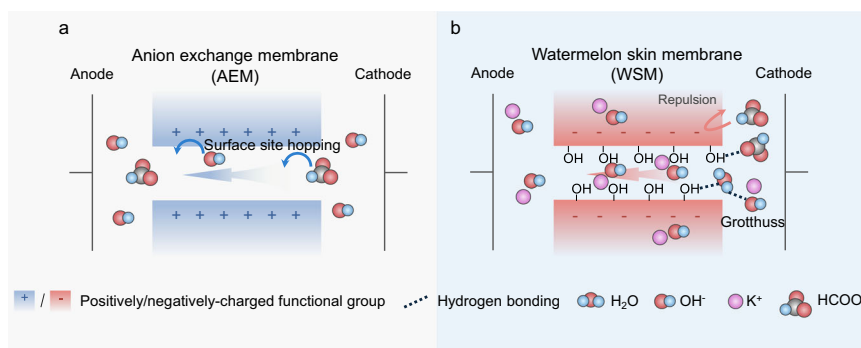


Fig. 1 | Illustration of the ion transport mechanisms. a The hopping transport mechanism in AEM membranes. **b** The ion-selective transport mechanism in WSM.

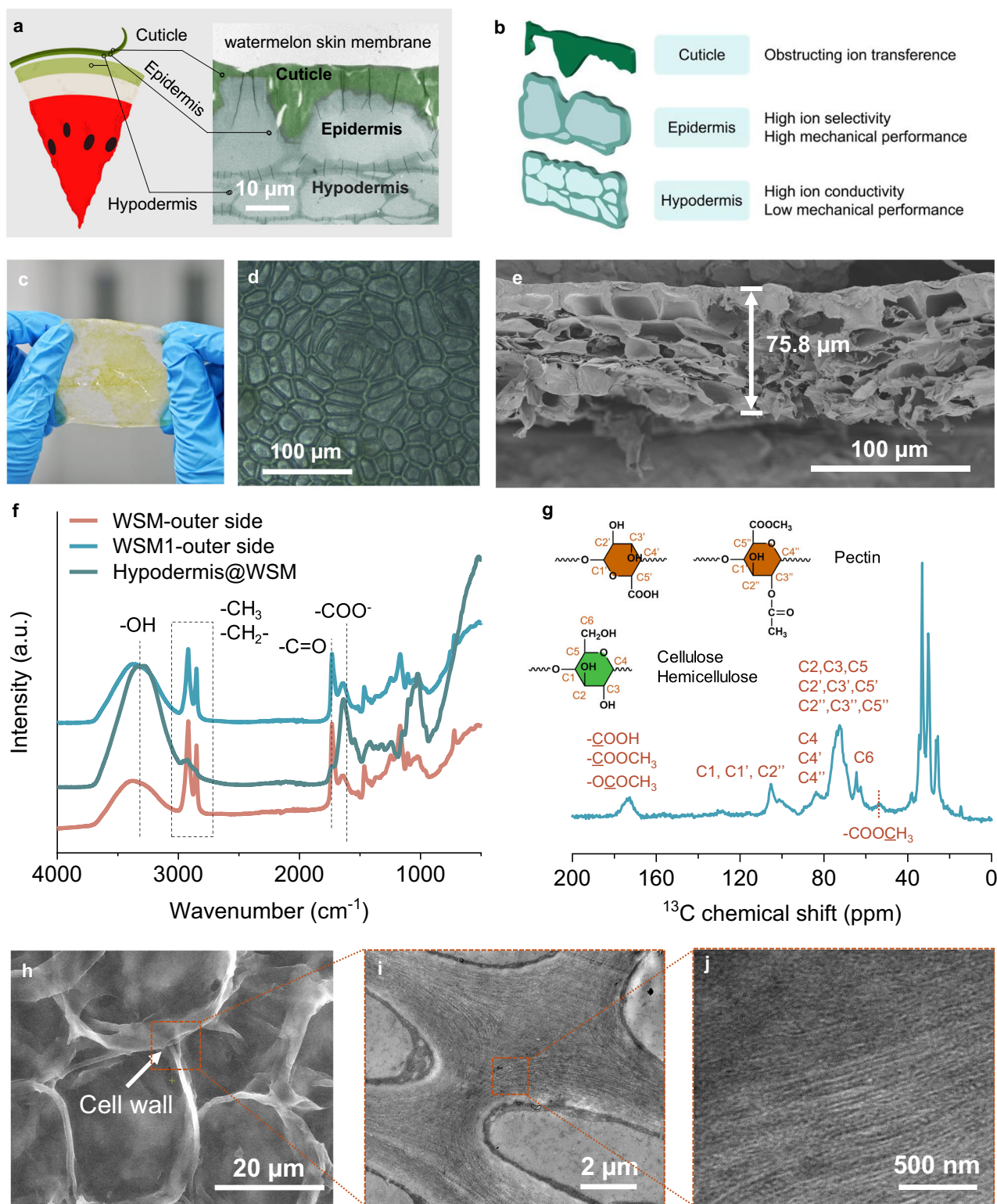


Fig. 2 | The structures and compositions of WSM. **a** Schematic of watermelon after application of the freezing-exfoliation method (*left*) and the TEM image (*right*) of the obtained WSM. **b** Illustration of the three layer structure of WSM and their functionality descriptions. **c** WSM obtained using the freezing-exfoliation method (thickness: 75 ± 5 μm). **d** Optical microscopic image of WSM. **e** Cross-sectional SEM

image of freeze-dried WSM. **f** FTIR spectra of WSM-outer side and Hypodermis@WSM. **g** Solid-state ¹³C NMR spectrum of WSM, and typical structures of cellulose/hemicellulose and pectin. **h** TEM image of the cell wall of WSM cells. **i** Magnified TEM image of the sample shown in **h**. **j** Magnified TEM image of the sample shown in **i**.

However, the peaks aforementioned are significantly weakened in Hypodermis@WSM, while the other peaks show no apparent changes. This indicates that there's no cuticle layer in the Hypodermis layer and SEM images substantiated this result (Fig. S1d, e). Atomic force

microscope (AFM) topography further illustrates that the morphologies of the outer and inner sides of the watermelon skin are completely different (Fig. S2). The peaks at 1610 cm⁻¹ and 3350 cm⁻¹ have been assigned to carboxylate (COO⁻) and -OH respectively⁴¹ and the higher

Table 1 | Characteristic physical parameters of the membranes analyzed in this study

| Membranes | Thickness (μm) | Tensile stress (MPa) | Tensile strain (%) | Water uptake (%) | Gas permeability ^a ($\text{cm}^3/\text{m}^2\cdot 24\text{ h}\cdot 0.1\text{ MPa}$) | | | Ion conductivity ^b (mS cm^{-1}) |
|----------------|-----------------------------|----------------------|--------------------|------------------|---|----------------|-----------------|---|
| | | | | | H ₂ | O ₂ | CO ₂ | |
| WSM | 75.0(± 5) | 6.1 | 13.3 | 470.9 | 2.4 | 5.7 | 8.9 | 49.1(± 2.5) |
| WSM1 | 70.0(± 3) | 4.7 | 14.1 | 482.1 | 2.6 | 5.8 | 8.7 | 101.2(± 1.0) |
| Hypodermis@WSM | 120(± 5) | 0.76 | 5.4 | 731.7 | / | / | / | 282.3(± 8.4) |
| Fumasep | 130.0 | 13.8 | 4.5 | 11.3 | 2.3 | 5.0 | 2.0 | 6.7(± 2.6) |
| Sustainion | 50.0 | 5.9 | 7.4 | 26.0 | 2.8 | 2.2 | 3.3 | 94.1(± 4.2) |
| QAPPT | 25.0 | 28.50 | 13.17 | 17.3 | 2.4 | 2.7 | 2.5 | 69.3 (± 6.5) |

^aTest standard: ASTM D3985-2017; membranes were swelled with DI water during the test.

^bMeasured at room temperature (RT) under a N₂ atmosphere saturated with 1 M KOH aqueous solution. The standard deviation was obtained from three individual experiments.

intensity of these peaks in the spectra of Hypodermis@WSM demonstrated that the cell wall contains more hydrophilic function groups than cuticle layer (Fig. S1c, f). The ¹³C chemical shifts at 170–180 ppm have been assigned to the carbonyl group (C=O) of COOH (176 ppm), acetyl (OCOCH₃), and methyl ester (COOCH₃) from hemicellulose and pectin. The shifts at 90–110 ppm are assigned to the ether group (R-O-R) from cellulose/hemicellulose and pectin³⁹. The chemical structures of cellulose, hemicellulose and pectin are shown in the Fig. S3.

Both the cell wall and the plasma membrane of plants could be the locations for the transport of water and ions (Fig. S4). The cell viability is identified by using propidium iodide (PI) as a fluorescent identification agent⁴². Red spots were detected inside the cells once a WSM prepared by the freezing-exfoliation method was treated with the PI solution in the dark for 20 minutes (Fig. S5), which indicates that the cells were dead, and plasma membranes were not integrated. Thus, the main ion-transport site of the WSM was the cell wall rather than the plasma membrane. The cell wall structure of WSM cells was characterized using SEM (Fig. 2h) and TEM (Fig. 2i, j). The cellulose fibers were arranged regularly, forming three-dimensional restricted channels with a diameter of 2–5 nm (Fig. S6), and pectin uniformly filled the regularly arranged three-dimensional fiber channels⁴³. This unique structure limits the volume swelling caused by the high-water-uptake pectin, which allows the WSM to have both good water absorption and mechanical stability.

The water uptake, mechanical strength, gas permeability, and ion conductivity are the main factors affecting the performance of ITMs. Hence, these physical parameters of WSM were investigated and compared with commercial benchmark AEMs, Fumasep FAB-PK-130 (Fumasep)^{44,45}, Sustainion X37-50 Grade T (Sustainion)^{10,46} and quaternary ammonia poly(N-methyl-piperidine-co-p-terphenyl) (QAPPT)⁴⁷. To accurately quantify the physical properties of the three layers of the WSM, detailed studies were conducted on three samples: WSM, WSM1, and Hypodermis@WSM (Fig. S7). Among them, WSM1 is a sample obtained by soaking the WSM sample in CHCl₃ for 72 hours and dissolving a portion of its surface cuticle (Fig. S7d)⁴⁸. The Hypodermis@WSM is a sample with a thickness of approximately 120 \pm 5 μm , exfoliated from the watermelon.

As shown in Table 1, the average water uptake of WSM, WSM1, and Hypodermis@WSM at room temperature is 470.9%, 482.1%, and 731.7%, respectively, all higher than the water uptake of Fumasep (11.3%), Sustainion (26.0%) and QAPPT (17.3%) under the same condition. WSM and WSM1 in a fully hydrated state exhibit good mechanical performance, with tensile stresses of 6.1 MPa and 4.7 MPa, and a strain at break of 13.3% and 14.1%, respectively, superior to Sustainion under the same conditions (5.9 MPa, 7.4%). Due to its woven structure, Fumasep is prone to local fracture during tensile deformation (Fig. S8 and S9) with a tensile stress of 13.8 MPa and a strain at break of only 4.5%. WSM and WSM1 maintain a balance between mechanical strength and water uptake, which is mainly attributed to the unique

structural features of the cell wall: highly water-absorbent pectin uniformly fills the weak hydrophilic three-dimensional nanochannels composed of cellulose, thereby restricting excessive volume expansion. According to the literature³⁶, it has been reported that the close and interlocking arrangement of cellulose in the cell wall structure of the epidermis layer contributes to its strong mechanical properties, which is consistent with the results of this experiment. Gas permeability is an important physical parameter for the membranes used for gas separation in electrolysis equipment, such as the anode and cathode gases. WSM and WSM1 have gas permeability similar to Fumasep, Sustainion and QAPPT for H₂, O₂, and CO₂, indicating their excellent gas permeation resistance. This study tested the through-plane ionic conductivity of the membranes, with specific testing methods detailed in the supplementary information. To validate the universality of this work, ion conductivity tests were carried out on two types of watermelon skins with thicknesses of 75 \pm 5 μm and 35 \pm 5 μm respectively. The results demonstrated that both samples exhibited similar ion conductivities (Fig. S10). The ionic conductivity of WSM1 (101.2 mS cm⁻¹) is approximately twice that of WSM (49.1 mS cm⁻¹). The ionic conductivity of Hypodermis@WSM (282.3 mS cm⁻¹) is approximately 5.5 times higher than that of WSM and also surpasses that of Fumasep (6.7 mS cm⁻¹), Sustainion (94.1 mS cm⁻¹) and QAPPT (69.3 mS cm⁻¹) under the same condition. These results demonstrate that the structure of the epidermis and hypodermis plays an important role in the high ion transport characteristics of the WSM. Additionally, because it is not affected by the cuticle of the epidermis, the ionic conductivity of Hypodermis@WSM is closer to the actual ion conductivity of the cell wall, higher than the ionic conductivity of 1 M KOH water solution (195.1 mS cm⁻¹) at room temperature⁴⁹.

Based on the above experimental data, the following conclusions can be drawn: (i) The ion conductivity of WSM1, with part of the cuticle layer removed, significantly increases, indicating that the presence of the cuticle layer impedes the ion transport of WSM; (ii) The unique structure of the epidermal layer gives it excellent mechanical properties; (iii) Hypodermis@WSM has an ion conductivity much higher than AEMs, indicating that the ion transport mechanism of cell walls is more efficient. Given the relatively similar mechanical properties and gas permeability of WSM and WSM1, but WSM1 exhibiting approximately double the ionic conductivity of WSM, our subsequent characterization and testing efforts within this study will primarily concentrate on WSM1.

Ion-transport channels in the cell wall

To investigate the intrinsic reason for WSM1 which exhibits excellent ion conductivity, in-depth experimental verification was conducted. Figure 3a shows a schematic diagram of the two possible pathways for OH⁻ transport in WSM1. Pathway 1 represents the transport of OH⁻ along the cell wall, while pathway 2 describes how OH⁻ can pass through the cell wall and the cell cavity filled with electrolytes. The ion conductivity

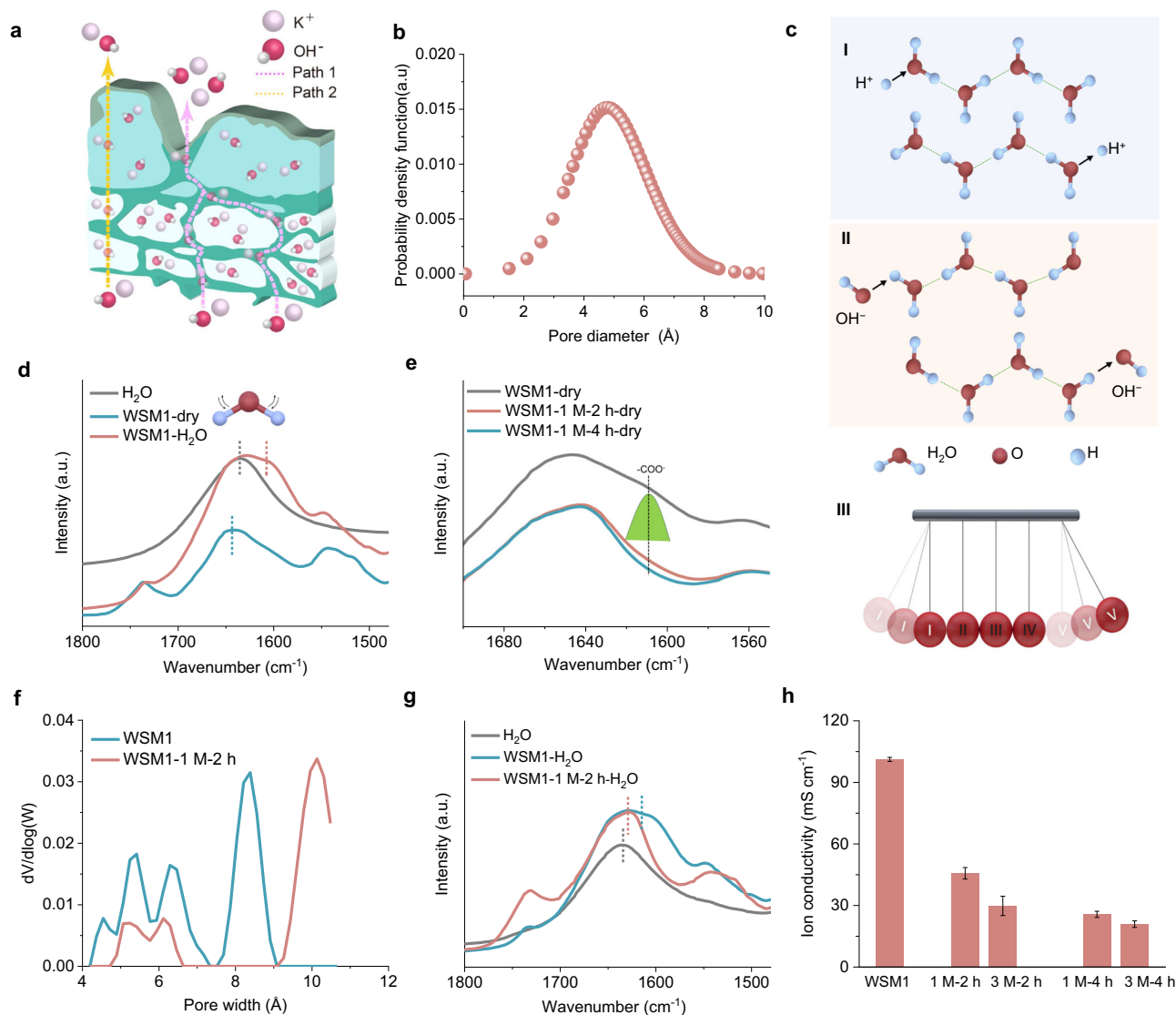


Fig. 3 | Ion-transport channels in the cell wall. **a** The schematic diagram of the transport pathway of OH^- in WSM1. **b** Pore size distribution of WSM1 obtained from PALS. **c** Schematic of the Grotthuss mechanism: proton transfer mechanism (I); hydroxides transfer mechanism (II); Schematic of Newton's cradle (III). **d** FTIR spectra of H_2O , WSM1- H_2O (WSM1 fully absorbed H_2O , and the surface H_2O was wiped off), and WSM1-dry (the dried WSM1). **e** FTIR spectra of the WSM1-dry, WSM1-1M-2h-dry (the WSM1 soaked in 1 M H_2SO_4 solutions for 2 h and then dried),

and WSM1-1M-4h-dry (WSM1 soaked in 1 M H_2SO_4 solutions for 4 h and then dried). **f** Pore size distributions of the WSM1 and WSM1-1M-2h-dry obtained from the BET method. **g** FTIR spectra of H_2O , WSM1- H_2O , and WSM1-1M-2h- H_2O (After soaking WSM1 in a 1 M H_2SO_4 solution for 2 hours, rinse it repeatedly with deionized water, dry it, and finally fully absorb H_2O). **h** Ion conductivity of WSM1 after acid treatment. The error bars represent the standard deviation of ion conductivity.

of Hypodermis@WSM in 1 M KOH electrolyte (282.3 mS cm^{-1}) is significantly higher than the intrinsic ion conductivity of 1 M KOH (195.1 mS cm^{-1}), suggesting that the ion transport channels within the cell wall can accelerate the transport of OH^- . To figure out the structure-activity relationship, both positron annihilation lifetime spectroscopy (PALS) and Brunauer-Emmett-Teller (BET) techniques were initially employed. The results (Fig. 3b, Fig. S11, S12) indicated that WSM1 possessed a microporous structure. According to previous reports, microporous polymers had a certain interchain gap size, which provided a low-hindrance transfer path for hydroxide^{7,9,50}.

The transport of protons and hydroxides in the water system is controlled by the Grotthuss mechanism, i.e., hydrogen-bonding network transport^{51,52}. The construction of continuous hydrogen-bonding networks is beneficial for accelerating the transport of protons and hydroxides (Fig. 3cI, Fig. 3cII)^{53,54}. For example, when protons are transmitted through a hydrogen-bonding network (Fig. 3cI), the proton bridging two hydrogen-bonded water molecules switch from one

molecule to the other, while kicking an existing proton out of its adopted molecule and triggering a series of resembles displacements through the continuous hydrogen-bonding networks. This motion is similar to Newton's cradle (Fig. 3cIII), where the associated local displacement leads to long-range proton transport.

Since the hydroxyl and carboxyl groups in cellulose and pectin are hydrophilic, water molecules are readily confined within the micropores constructed by cellulose and pectin. Additionally, hydroxyl and carboxyl groups are proton donors. Concentrated hydrated hydrogen ions can be inferred to induce the rearrangement of water molecules of enclosed water near hydroxyl and carboxyl groups, thereby promoting the formation of a continuous hydrogen-bonding network⁵⁵ and accelerating the proton/ hydroxides transport rate.

FTIR was used to investigate whether the WSM1 contained continuous hydrogen-bonding networks. As shown in Fig. S13, in the water system, H_2O molecules have two distinct characteristic vibration peaks at 1638 cm^{-1} and 3300 cm^{-1} , which are attributed to the bending

vibration of the O-H bond and the stretching vibration of the O-H bond, respectively⁵⁵. Due to the large amount of -OH in the WSM1-dry, the characteristic vibration peak at 3300 cm⁻¹ coincides with the 3300 cm⁻¹ peak in the H₂O system and has a wider peak width (Fig. S14). Thus, to explore whether continuous hydrogen-bonding networks were formed, the offset of the bending vibration peaks at 1638 cm⁻¹ of the O-H bond in three samples of H₂O, WSM1-dry and WSM1-H₂O were chosen for comparison. As shown in Fig. 3d, a characteristic vibration peak was found at 1612 cm⁻¹ in the WSM1-H₂O system, with a redshift relative to the bending vibration peak of the O-H bond in the H₂O system. This redshift was due to the increased stiffness of the O-H bond bending mode caused by the electrostatic force between H and the acceptor atoms after the formation of continuous hydrogen-bonding networks⁵⁶. Therefore, continuous hydrogen-bonding networks formed in the WSM1, which is beneficial for accelerating H⁺/OH⁻ transport.

Since the main components of WSM1 are cellulose and pectin, we prepared cellulose and pectin membranes using commercially available cellulose and pectin, respectively. After water absorption, the bending vibration frequency of the O-H bond in these two types of membranes did not show a redshift compared to the pure water system (Fig. S15a, b), which indicated that continuous hydrogen-bonding networks were not formed in these two membrane structures⁵⁷. Therefore, disordered hydroxyl-rich polymer structures have difficulty forming continuous hydrogen-bonding networks.

To investigate the role of pectin in the formation of micropores and continuous hydrogen-bonding networks in the WSM1, we performed pectin removal treatment on the WSM1. According to the literature⁴¹, the dissolution of pectin can be accelerated in an acidic medium at 60 °C. Therefore, we soaked WSM1s in 1 M H₂SO₄ solutions and placed them in a 60 °C oven for 2 (Figs. S16) or 4 hours. Figure 3e shows the FTIR spectra of the WSM1s before and after H₂SO₄ treatment. According to the spectrum, the intensity of the peak at 1610 cm⁻¹, which is the characteristic vibration peak of -COO⁻ in pectin⁴¹, significantly decreased. Solid-state ¹³C NMR spectra of WSM1 and WSM1-1 M-2 h also demonstrated that the signal of pectin has decreased after H₂SO₄ treatment (Fig. S17). This suggests that the pectin content of the WSM1 decreased after acid treatment. The microporous volume of the WSM1 after pectin dissolution increased (Fig. 3f), and their adsorption capacity for CO₂ gas significantly decreased (Fig. S18). Through FTIR characterization, it was observed that WSM1-1 M-2 h exhibited a redshift decrease in the peak at 1638 cm⁻¹ relative to untreated WSM1, as illustrated in Fig. 3g. This indicated that after pectin dissolved, the hydrogen-bonding strength weakened. At the same time, the dissolution of pectin also caused a significant decrease in the ion conductivity of the WSM1 (Fig. 3h). The above experiments indicate that (i) pectin plays an important role in the formation of micropores and continuous hydrogen-bonding networks in cell walls and (ii) micropores and continuous hydrogen-bonding networks constructed by the synergistic effect of pectin and cellulose are crucial for improving ion-transport efficiency.

Ion selective permeation of WSM1

A prominent issue arises from the crossover of anionic CO₂ reduction products, such as formic acid, acetic acid, and propionic acid, occurring through the electromigration process within the AEMs^{10,25}. An ideal ITM used for CO₂RR should have excellent ion selectivity. Here, we selected five common liquid products from the CO₂RR for ion selectivity testing of WSM1. The electrochemical measurement system for the CO₂RR liquid product crossover test of WSM1 is shown in Fig. 4a. Five common liquid products of the CO₂RR^{58,59}, i.e., formic acid, acetic acid, propionic acid, ethanol, and propanol, were added to the catholyte, and the system was operated for 5 hours with no CO₂ reactant at a current density of 200 mA cm⁻². The catholyte was collected at different intervals and analyzed using ¹H NMR.

As shown in Fig. 4b–f, when Fumasep/Sustainion/QAPPT was used as the ITM, the crossover rates of the formate, acetate, propionate, ethanol, and propanol were 64.0%/47.4%/58.75%, 42.3%/31.8%/42.99%, 17.7%/30.4%/42.43%, 6.8%/26.4%/21.28%, and 7.2%/24.8%/24.38%, respectively. In contrast, when WSM1 was used as the ITM, the crossover rates of the same liquid products were 5.0%, 5.6%, 8.9%, 6.1%, and 1.6%, respectively. The crossover rate of formate for WSM1 was approximately 12.8/9.6/11.8 times lower than that for Fumasep/Sustainion/QAPPT when used under the same conditions. Thus, the WSM1 exhibited excellent ion selectivity compared to Fumasep, Sustainion, and QAPPT.

A detailed comparison was conducted among WSM, WSM1, and Hypodermis@WSM regarding ion selectivity. As shown in Fig. 4b–f, WSM, WSM1, and Hypodermis@WSM exhibited excellent ion selectivity for common ion products in CO₂RR. However, Hypodermis@WSM displayed a slightly lower ion selectivity compared to the other two. The epidermis layer exhibits the most exceptional ion selectivity. We conducted a detailed analysis of the cellulose and pectin content in WSM1 and Hypodermis@WSM. The mass ratio of pectin to cellulose in WSM1 was 0.067, while in Hypodermis@WSM, it was 0.024. This indicates that the mass ratio of pectin to cellulose in the epidermal layer is greater than 0.067. Therefore, among the three layers of the watermelon skin, the epidermal layer has the highest pectin content. Because pectin contains an abundance of negatively charged groups, it has the ability to repel acid anions, resulting in excellent ion selectivity within the epidermal layer.

With WSM1-1 M-2 h (with partial pectin removed) employed as the ITM, the crossover rates of formate, acetate, propionate, ethanol, and propanol were higher than those of the untreated WSM1 (Fig. 4b–f). This indicates that the partial removal of pectin reduces the ion selectivity of WSM1. To verify the inhibitory effect of negative charge groups on acid anions, we chose Nafion115 PEM, which has a large number of sulfonic acid groups, for ion-selective permeation experiments. The experimental results are shown in Fig. S19. Compared with Fumasep, Nafion115 has a lower permeation rate of acid anions, indicating that negative charge groups can inhibit the permeation of acid anions. In addition, we also found that WSM1 has better ion selectivity than Nafion115. Accordingly, there are two main reasons why the WSM1 exhibits good ion selectivity: (i) the carboxyl groups in pectin are negatively charged and thus repel negatively charged ions such as HCOO⁻ and CH₃COO⁻ and (ii) although the many hydroxyl groups in the WSM system bind with OH⁻ and acid ions through hydrogen bonding, OH⁻ could be transferred through the continuous hydrogen-bonding networks, whereas acid ions could not.

To further theoretically demonstrate the above conclusion, we conducted molecular dynamics simulations on the WSM1 system. Two models were constructed: one with cellulose channels filled with pectin (Fig. 4g) and another with cellulose channels without pectin (Fig. S20). Both models included a formate molecule within the channel. Molecular dynamics simulations were employed to investigate the migration pathway of formate^{60–62}. In the system containing pectin, formate was initially located inside the simulated channel, while the center of mass of the entire simulated unit was located at the origin. The channel spanned approximately 95 Å in total length along the *x*-axis. Therefore, if the *x*-coordinate of the formate molecule exceeded the range of -47 to 47 Å, the formate molecule entered the adjacent unit. As shown in Fig. 4h, in the pectin-containing model, the formate molecule oscillated back and forth at varying speeds throughout the entire 400 ns simulation time. The start and end positions of the formate molecule in the simulation were both within the original simulation unit. In the pectin-free model system (Fig. 4i), the formate molecule experienced a significant shift in the negative field strength direction. The formate molecule tended to move vertically toward the cellulose channel wall and interact with the hydroxyl group of the sugar ring through hydrogen bonding, which restricted

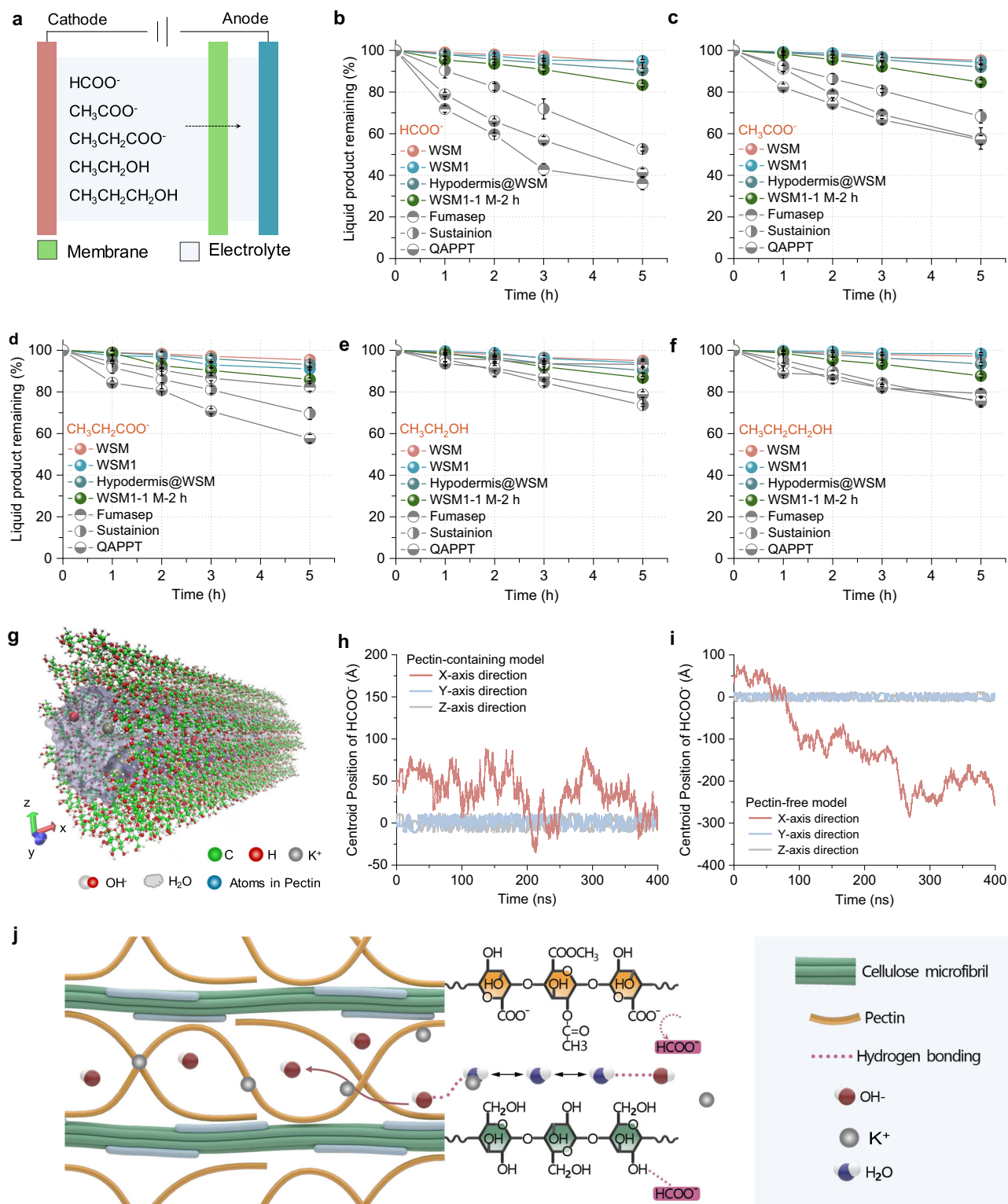


Fig. 4 | Ion selective permeation of WSM1. a Schematic diagram of the liquid product crossover test device. **b–f** Remaining ratios of formate, acetate, propionate, ethanol, and propanol in the catholyte when WSM, WSM1, Hypodermis@WSM, WSM1-1 M-2 h (the WSM1 soaked in 1 M H_2SO_4 solutions for 2 h), Fumasep, Sustainion or QAPPT was used as the ITM. The error bars represent the

standard deviation of the remaining ratios. **g** Pectin-containing model diagram for molecular dynamic simulation. **h** Position of formate in pectin-containing systems as a function of the simulation time. **i** Position of formate in a pectin-free system as a function of the simulation time. **j** Mechanism diagram of selective permeation of WSM1.

its movement. However, the interaction between the formate molecule and the hydroxyl group of the sugar ring was not very strong, so the formate molecule was easily detached and re-incorporated into the solvent. The formate continued to move under the influence of the

electric field. The above results indicate that pectin rich in $-\text{COO}^-$ functional groups repelled HCOO^- and reduced its transmission. Thus, the calculation simulation yielded consistent results with the experimental findings.

From the above experimental and modeling results, we formulated the ion transport mechanism in the WSM1: OH⁻ is accelerated through the continuous hydrogen-bonding networks and microporous channels, while acid ions are repelled by negatively charged groups in pectin and form certain hydrogen bonds with hydroxyl groups, making penetration through the WSM1 difficult (Fig. 4j). This is the fundamental reason why WSM1 has both high ion conductivity and excellent ion selectivity.

Performance of the CO₂RR system with WSM1

The high ion conductivity and low CO₂RR liquid product crossover behavior of WSM1 make it particularly suitable for CO₂RR systems. Thus, we evaluated the performance of the WSM1 for the CO₂RR utilizing a currently widely used electrochemical flow cell system (Fig. 5a, Fig. S21, S22) in which the cathode catalyst was previously reported to be CoPc⁶³, while NiFeOOH⁶⁴ was used as the anode catalyst. The cell voltages for CO production applied on the two electrodes at different current densities were measured without iR compensation. Online gas chromatography was used to detect and quantify the evolution of the electrolytic products CO over a current density range of 100–500 mA cm⁻². When 1 M KOH was used as the electrolyte (Fig. 5b), the average cell voltages of WSM1 at 100 mA cm⁻², 200 mA cm⁻², and 500 mA cm⁻² are 2.30 V, 2.56 V, and 2.98 V, respectively, significantly lower than Fumasep but comparable to Sustainion / QAPPT. The average cell voltages of Hypodermis@WSM at 100 mA cm⁻², 200 mA cm⁻², and 500 mA cm⁻² are 2.12 V, 2.25 V, and 2.55 V, respectively, significantly lower than Sustainion, QAPPT and Fumasep. Furthermore, at current densities ranging from 100–500 mA cm⁻², both WSM1 and Hypodermis@WSM maintain a CO Faradaic efficiency (FE_{CO}) of approximately 90%. The device that employs WSM1 as the ISM can run stably for approximately 115 hours (RT, Fig. 5c) at a current density of 100 mA cm⁻² and with 1 M KOH as the electrolyte. These data indicate that the ion transport channels in the cell wall of watermelon skin have remarkable ion transport capabilities and can serve as a benchmark for artificial biomimetic membranes.

Furthermore, the FE was evaluated at a current density of 200 mA cm⁻² (Fig. 5d), and was monitored at the first, third, and fifth hours during the reaction with copper serving as a cathode catalyst (Fig. S24). The system comprised both gaseous and liquid products, and the total FE was maintained at ~95% for over 5 hours (Fig. 5e), which indicates that the application of WSM1 in the CO₂RR system is beneficial for collecting cathode products and objectively evaluating the performance of cathode catalysts.

Discussion

In this work, we investigate the structure-activity relationship of a natural WSM. In contrast to the traditional AEM system, WSM as an ISM no longer relies on the surface site hopping mechanism but instead utilizes the absorption of aqueous alkaline electrolyte to transport hydroxide (Fig. S25). High-water-uptake pectin network is uniformly filled in ordered spatial channels (2–5 nm) composed of cellulose fibers. The micropores (~5 Å) containing organized hydroxyl groups that form continuous hydrogen-bonding networks facilitate the hydroxide to overcome the repulsion of carboxyl groups via the Grotthuss mechanism. The negatively charged functional groups restrict the migration of other acid ions through the charge repulsion and hydrogen bond drag forces. These characteristics make WSM1 and Hypodermis@WSM demonstrate excellent ion conductivity (up to 282.3 mS cm⁻¹, RT, saturated with 1 M KOH) and anionic selectivity. Both membranes achieve a high current density of 500 mA cm⁻² when the average voltage in the CO₂RR flow cell is 2.98 V and 2.55 V, respectively. Furthermore, the formate crossover rates of WSM1 are ~12.8 times and ~9.6 times lower than those of Fumasep and Sustainion, respectively.

Based on the findings of this study, the following strategies are proposed for the design of high-performance ISMs: (i) Constructing nanochannels to enhance hydroxide transport efficiency by designing three-dimensional ordered framework structures; (ii) Establishing high-speed ion transport channels with ion selectivity by confining ultra-microporous polymers rich in proton donors and negatively charged groups within a three-dimensional framework structure.

However, due to the complex structure and composition of biomass in the cell wall, this study's analysis of ion transport mechanisms in WSM needs to be more comprehensive in the following investigation. Further research also could be focused on the permeability of other substances, such as biomass/biomass intermediates, not limited to common liquid products of CO₂RR. In summary, this work offers valuable insights into the ion transport mechanism in biofilms and inspires to design advanced ISMs.

Methods

Materials

Cobalt phthalocyanine (CoPc) (>97%) was purchased from Tokyo Chemical Industry CO., Ltd., and potassium hydroxide from General-Reagent. Iron (III) nitrate nonahydrate (>98%) and the Nafion 117 solution from Aladdin, 1-Ethyl-3-methyl-3-imidazolium Acetate (EMIMAc) (>98%) from Alfa Chem, sodium sulfite (>97%) from Innochem, cellulose and pectin from Sigma, Poly (vinyl alcohol) (PVA) (>98%) from TCI. The polytetrafluoroethylene (PTFE) gas diffusion layer with 450 nm pore size was purchased from Gaoss Union (Tianjin) Photoelectric Technology Co., Ltd. And the carbon powder (Vulcan XC-72R) from Fuel Cell Store. The standard Potassium hydroxide solution (1 mol/L, pH=13.68 ± 0.03) was purchased from Shenzhen Bolinda Technology CO., Ltd. All chemicals were used as received without further purification. Anion exchange membrane (AEM) Fumasep®FAB-PK-130 was purchased from Fumatech CO., Ltd., Sustainion X37-50 Grade T from Dioxide Materials, and QAPPT from Evehydrogen CO. The watermelon with an average skin thickness 75 ± 5 μm was produced in Ningxia province, China. The watermelon with an average skin thickness of 35 ± 5 μm is 8424 kirin melon purchased from the supermarket in Hangzhou.

Experimental methods

Flow cell assembly. The electrolyzer cell depicted in Fig. S21 was purchased from Gaoss Union (Tianjin) Photoelectric Technology Co., Ltd. The distance between the two electrodes is 0.7 mm. One compartment delivers the CO₂ (at 20 standard cubic centimeters per minute (SCCM)) from the back side and through the gas diffusion electrode (GDE, 2 × 0.5 cm²), while another directs the catholyte solution (1 M KOH, flow rate of 40 SCCM) between the GDE and the ion-transport membrane (Watermelon skin, Fumasep®FAB-PK-130). On the other side of the membrane, the anolyte (1 M KOH, flow rate of 80 SCCM) was directed between the membrane and the anode catalyst. The flow frames are made of PTFE, and the gaskets of peroxide cured ethylene propylene diene monomer rubber. Catholyte and anolyte were recycled via peristaltic pumps.

Preparation of watermelon skin membrane. The watermelons were placed in a freezing chamber of a freezer overnight at around -20 °C, and then thawed naturally at room temperature. After thawing, the skin was peeled off by hands.

Preparation of cellulose membrane, pectin membrane, and PVA membrane

Cellulose membrane. The method for preparing the cellulose membrane was modified in accordance with a reported work⁶⁵. Cellulose powder (100 mg) was obtained and vacuum-dried at 80 °C for 12 hours. Afterward, it was dissolved in the ionic liquid EMIMAc (1-Ethyl-3-methyl-3-imidazolium Acetate) to formulate an 8 wt% film-

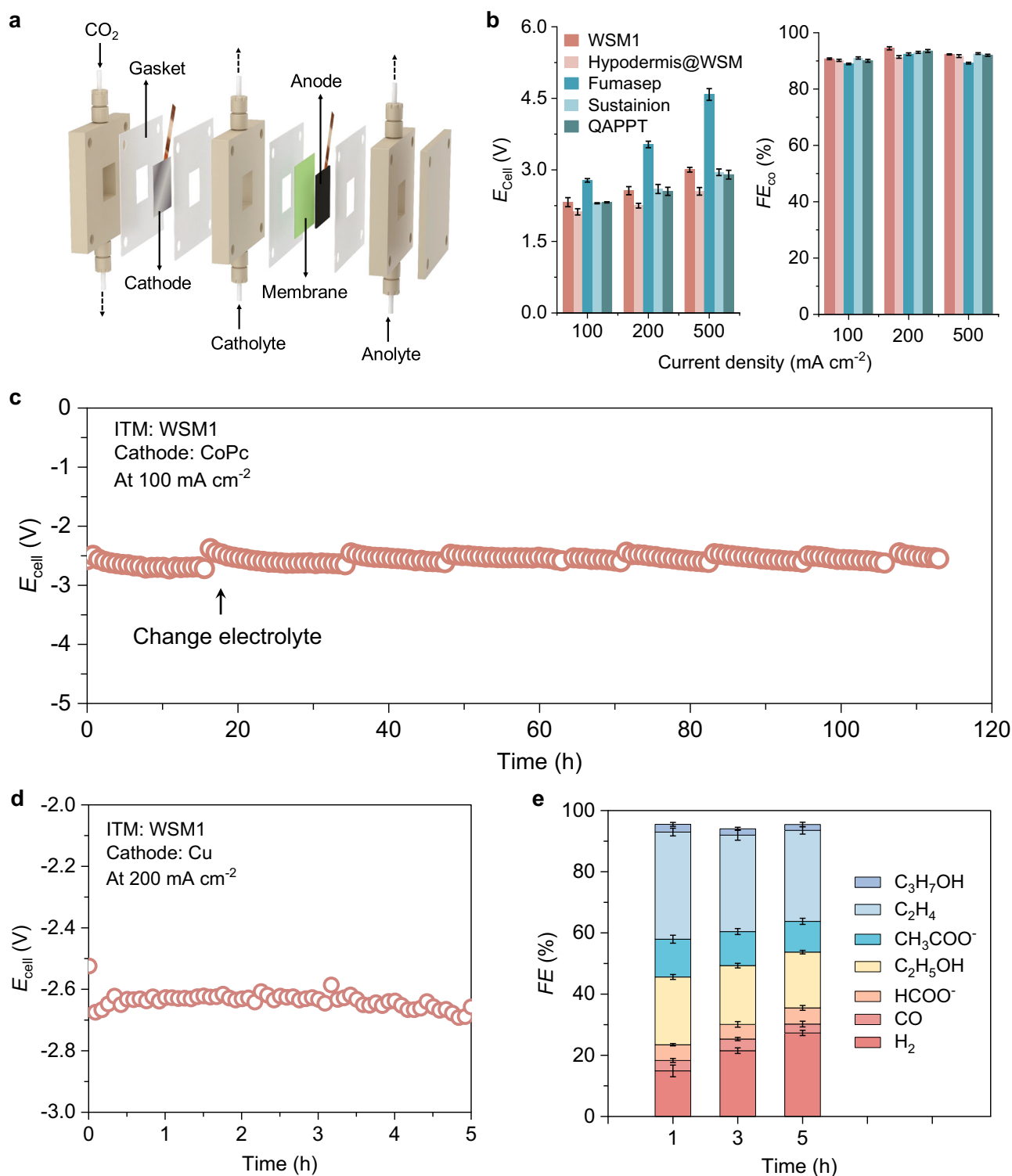


Fig. 5 | The performance of the CO₂RR system with WSM1 as ISM. a Schematic diagram of the CO₂ reduction device. **b** Applied cell voltage and CO₂RR selectivity for CO formation as a function of the current density with different membranes using 1 M KOH as electrolyte. Cathode catalyst: 2.0 mg/cm² CoPc loading on PTFE/Cu; anode catalyst: NiFeOOH. The error bars represent the standard deviation of E_{cell} and FE_{CO} . **c** Temporal stability of the CO₂RR system with WSM1 as the ISM at

100 mA cm² using 1 M KOH as electrolyte. Cathode catalyst: 2.0 mg/cm² CoPc loading on PTFE/Cu; anode catalyst: NiFeOOH. **d** The cell voltage curve recorded for the CO₂RR system with WSM1 as the ISM operating at a current density of 200 mA cm². **e** FE of the CO₂RR system with WSM1 as the ISM at a current density of 200 mA cm² using 1 M KOH as electrolyte. Cathode catalyst: PTFE/Cu; anode catalyst: NiFeOOH. The error bars represent the standard deviation of FE.

casting liquid. The mixture was stirred in a thermostatic bath at 70 °C until the cellulose was entirely dissolved. Next, the solution was poured onto a glass plate. Five minutes later, the glass was immersed in deionized water for phase separation. Once the film was formed, it was rinsed with deionized water to eliminate the residual ionic liquids.

Pectin membrane. Pectin (100 mg) was dissolved in deionized water (5 mL) and stirred to achieve completely dissolve in a glass bottle. The solution was filtered and poured onto a PET plate for 12 hours at 40 °C to obtain an intact membrane.

PVA membrane. PVA (100 mg) was dissolved in deionized water (5 mL) and stirred to achieve complete dissolution in a glass bottle. The solution was filtered and poured onto a PET plate and kept for 12 hours at 40 °C to obtain a transparent membrane.

Electrode preparation

Cathode. Cu was sputtered onto the PTFE substrate (PTFE/Cu) via pure Cu targets (>99.99%) in a vacuum environment (10^{-5} – 10^{-6} Torr) with a Load-lock type Sputtering System. The thickness of the catalyst layer was kept constant for all the electrodes around 300.0 nm with 360.0 s deposition time. The cobalt phthalocyanine (CoPc) ink was prepared by stirring and sonicating 82.9 mg of Vulcan carbon powder, 89.6 mg of CoPc, and 1122 μ L of Nafion 117 solution (5.0 wt% in a mixture of ink was spray-coated on PTFE/Cu). The resulting electrode was 30.0 cm². The CoPc concentration was expected to furnish a 2.0 mg/cm² CoPc loading after spray coating.

Anode. The method for preparing the anode was referred to the previously reported work⁶⁴. The porous NiFeOOH catalysts were fabricated on Ni mesh through a one-step solution-phase method at room temperature. The solution was prepared by dissolving 0.562 g of Fe(NO₃)₃·9H₂O and 0.086 g of Na₂S₂O₃·5H₂O into 10 mL of DI water in a small glass bottle. Subsequently, one piece of commercial Ni mesh (1.0 × 3.0 cm²) was placed in the solution. After 10 minutes, the color of the Ni mesh shifted from its original metallic luster and turned darker as the reaction time increased. The sample was then taken out of the solution, washed multiple times with deionized water, and dried in the air before undergoing electrochemical testing.

Through-plan (TP) membrane conductivity measurements. The TP conductivity was measured through a straightforward method as follows⁶⁶. One piece of the membrane was placed between two round Pt tablets with diameters of 0.2 cm and 0.1 cm respectively. The surfaces of the Pt tablets were polished to be extremely smooth and flat. The Pt sheets were connected to the electrochemical impedance spectroscopy (EIS) testing station (CHI instruments 760) for resistance measurement. Measurements were carried out with an average AC voltage of 0 V and an amplitude of 0.1 V within a frequency range from 1 MHz to 1 Hz. Subsequently, the hydroxide conductivity (σ) was calculated using Eq. (1).

$$\sigma = T / (R^*A) \quad (1)$$

where σ (S cm⁻¹) represents the TP membrane conductivity. T (cm) indicates the membrane thickness. R (Ω) is the resistance of the membrane, and A (cm²) is the effective area of the membrane, which is the area (diameter of 0.1 cm) of the Pt tablet in this method. The membranes were balanced in 1 M KOH aqueous solution purged with N₂ gas for at least 24 h at room temperature before measurements.

Water uptake measurements. The method for measuring the water uptake was referred to the previously reported work⁶⁷. The determination of water uptake was achieved by measuring the weight

difference of the membrane before and after its immersion in deionized water. The samples were put in deionized water at the desired temperatures for 4 hours. They were dried with a kimwipe to eliminate the surface water and weighed promptly to determine the weight of the wet membrane. Subsequently, the wet membranes were dried at 60 °C under vacuum for 12 h and weighed once more to obtain the weight of the dried samples. The weights of the hydrated, W_{wet} , and dry, W_{dry} , membranes were then employed to calculate water uptake through the use of Eq. (2).

$$\text{Water uptake(\%)} = (W_{\text{wet}} - W_{\text{dry}}) / W_{\text{dry}} \times 100 \quad (2)$$

Testing of CO₂RR liquid products crossover. With the flow cell (Fig. S21) being the test device, the cathode is PTFE/Cu, the anode is NiFeOOH, and the electrolyte is 1 M KOH. Take 10 mg of the five common CO₂RR liquid products, such as formic acid, acetic acid, propionic acid, ethanol, and propanol, respectively, and add them to 40 mL of the cathode electrolyte. In the absence of CO₂ reactants, operate at a cell voltage of 200 mA/cm² for 5 hours, during which the cathode electrolyte was collected at intervals. With DMSO used as an internal standard, the transmittance of the above five liquid products was quantitatively determined through the nuclear magnetic resonance (NMR) analysis of the cathode electrolytes collected at different time periods.

Characterization of the samples in this work. Surface morphology was characterized by a Field Emission Environment Scanning Electron Microscope (ESEM, LHA20030057, Czech). In-situ observation is possible at ESEM mode (up to 4000 Pa), along with other tunable “real world” chamber conditions, including temperature, humidity, and partial pressure of reactive gases. In this work, the temperature is 2 °C, humidity is 85%, and partial pressure is 600 Pa. Transmission electron microscope (TEM, Thermo Fisher Scientific Talos 120 KV, America) was observed at 80 kV/120 kV in a FEI Talos 120 kV transmission electron microscopy operated at an acceleration voltage of 150 kV. Fourier transform infrared spectroscopy (FTIR, Thermo Fisher Scientific LHA19100028, China) was acquired on a spectrometer (Bruker EQUI-NOX55, Germany). Solid-State NMR (MAS Probe, Bruker BioSpin LHA19120049, Switzerland) experiments were carried out on Bruker Avance NEO 500 MHz spectrometer equipped with a 3.2 mm HXY triple-resonance MAS probe. One-dimensional (1D) ¹³C magic-angle spinning (MAS) spectrum was acquired under a spinrate of 20 kHz with 115 kHz high-power decoupling on the proton channel. Spectral line shape deconvolution in Bruker Topspin 4.1 software was applied to analyze the overlaid carbon peaks in the aromatic region. An optical microscope (Leica DM4M, Germany) was used to observe the high-resolution imaging for tissue sections, fluorescent labeling of biological materials, and fluorescent labeling of living cells. DUO micro-sourced Single Crystal X-Ray Diffractometer (GIWAX, Bruker LHA19090026, Germany) used a high-intensity diamond-blended X-ray light source. The exposure time was 180 s and the work distance was 60 μ m. The zeta potential of the watermelon skin was measured using a NanoBrook ZetaPALS. Freeze-dryer (Christ, ALPHA 2-4 LD PLUS, Germany) was used to preserve cell morphology while removing sample moisture. The pore width and carbon dioxide (CO₂) sorption of watermelon skin were performed on surface area analyzer gas adsorption/ desorption (Micromeritics) at 273.15 K. Positron annihilation lifetime spectroscopy (PALS) (Thermo Fisher Scientific, America) was used to obtain the microcavity size and free volume in the watermelon skin. It is important to emphasize that the watermelon skin samples used for the pore width and CO₂ sorption testing or the PALS testing were extracted from the freezing-exfoliation method and processed through freeze-drying. The content of pectin in watermelon skin was determined by using the carbazole colorimetric method. The

cellulose content in watermelon skin is determined using the Van Soest method.

Identification of live and dead state of watermelon skin cells. A watermelon skin with a size of 0.5 cm² was put into 100 μ L 0.9% NaCl solution. Then 50 μ L of 15 μ M propidium iodide was added to the aforementioned solution on the orbital shaker in the dark. Fluorescence intensity was measured with a Motorized Fluorescence Microscope (SONY) using a 645/40 nm (PI emission wavelength) emission filter.

Pectin removal. The watermelon skin was soaked in different concentrations of H₂SO₄ solution and placed at 60 °C oven for different times. Subsequently, rinsed with deionized water multiple times before use.

Electrolysis and product analysis

Electrochemical measurements were carried out at room temperature and pressure using a potentiostat (Altolab) via two-electrode cell measurements. The purchased flow cell has a fixed electrode geometric area of 2 \times 0.5 cm², two peristaltic pumps connected to the flow cell with silicone tubing, and a digital mass flow controller. The electrolyte solutions were freshly prepared with milli-Q water. The voltage presented in this paper is not compensated.

The gas products were harvested from the gas outlet channel of the flow cell and infused into a gas chromatograph (9790Plus). The gas chromatograph was outfitted with a thermal conductivity detector (TCD) for the detection of H₂ and O₂ signals and a flame ionization detector (FID) for the detection of CO, CH₄, C₂H₆, C₂H₄, and C₂H₂ signals. Argon (Linde, 99.999%) was employed as the carrier gas. For quantification, 1 mL of the gas product was injected into the gas chromatograph, and the performance was evaluated in relation to current density, gas flow rate, and gas product fraction.

$$\text{Faradaic efficiency}(\%) = N \times F \times v \times r / (i \times V_m) \quad (3)$$

where N is the number of electrons transferred, F is the Faradaic constant, v is the gas flow rate measured by soap bubble flow meter, r is the concentration of detected gas product in ppm, i is the total current, and V_m is the unit molar volume of gas. The gas flow rate was measured at the outlet of the gas chamber by a bubble flow meter.

Computing methods

Modeling. The initial model was constructed via the alpha-cellulose crystal structure unit (CCDC ID: JINROO05) determined experimentally. These crystals undergo cell expansion operations through Materials Studio, forming fiber bundles of specific lengths composed of four sugar chains; then, based on these fiber bundles, cellulose channels with different pore sizes are constructed separately. The initial model of pectin composite calcium ions was manually constructed using the composition shown in Fig. S20 as a template using Discovery Studio Visualizer. Furthermore, in the simulated systems containing pectin, the constructed pectin calcium complex was placed on the inner wall of the cellulose channel to form the final composite model. For comparison, we also constructed a pure aqueous solution of KOH. In all systems, the concentration of KOH is 1 mol/L.

Molecular dynamics simulation. All molecular dynamics simulations were conducted with the aid of the NAMD 2.14 software package. The force field parameters of cellulose and pectin are derived from the CHARMM36 sugar parameter set, while the force fields of formate ions are derived from the CGenFF force field. Periodic boundary conditions are used in the simulation. The short-range interaction gradually decreases to 0 in the range of 10–12 Å. The half price for team list search is set to 14 Angstroms. The calculation of long-range

electrostatic interactions uses the PME method⁶⁸. The dynamic simulation temperature is set to 298 K, and a Langevin hot bath is used for temperature control. Before starting the dynamic simulation, perform 50000 steps of conjugate gradient energy minimization to eliminate the high-energy contact area of the system; then an initial equilibrium simulation of 10 ns is carried out at a time step of 1 fs to obtain a more stable simulation system. After that, all chemical bonds containing hydrogen atoms are limited by the SHAKE rule, and the integration step is switched to 2 fs to carry out a re-equilibration process of 20 ns; In the subsequent output simulation stage, maintain the dynamic settings of the previous step and increase the field strength to 3.125 $\times 10^4$ mV/Å in the specified direction and continue the dynamic simulation of 400 ns. The obtained dynamic trajectory is used to calculate the velocity of ion motion.

Analysis of ion motion velocity. To ensure statistical regularity, we analyzed the average motion velocity of formate radical in each system under the action of an electric field, that is, selecting the centroid positions of all ions and calculating the motion velocity of the centroid. Due to the motion of particles within the channel, they are limited in the direction perpendicular to the channel, so only the velocity of motion along the channel direction is considered in the calculation. A self-designed calculation script was utilized within the TkConsole of VMD to analyze the trajectory of the above output simulation stage and perform the speed calculation.

Data availability

The authors declare that the data supporting the findings of this study are available within the paper, Supplementary Information, and Source Data files. Further data beyond the immediate results presented here are available from the corresponding authors upon request. Source data are provided with this paper.

References

- Zhu, P. & Wang, H. T. High-purity and high-concentration liquid fuels through CO₂ electroreduction. *Nat. Catal.* **4**, 943–951 (2021).
- Nitopi, S. et al. Progress and perspectives of electrochemical CO₂ reduction on copper in aqueous electrolyte. *Chem. Rev.* **119**, 7610–7672 (2019).
- Yu, Z. O., Duan, Y., Feng, X. U., Yu, X. & Yu, S. Clean and affordable hydrogen fuel from alkaline water splitting: past, recent progress, and future prospects. *Adv. Mater.* **33**, 2007100 (2021).
- Zhang, B., Fan, L., Ambre, R. B., Liu, T. & Sun, L. Advancing proton exchange membrane electrolyzers with molecular catalysts. *Joule* **4**, 1408–1444 (2020).
- Li, D., Park, E. J., Zhu, W., Shi, Q. & Yu, S. K. Highly quaternized polystyrene ionomers for high performance anion exchange membrane water electrolyzers. *Nat. Energy* **5**, 1–8 (2020).
- Wu, M. et al. A high-performance hydroxide exchange membrane enabled by Cu²⁺-crosslinked chitosan. *Nat. Nanotechnol.* **17**, 629–636 (2022).
- Song, W. et al. Upscaled production of an ultramicroporous anion-exchange membrane enables long-term operation in electrochemical energy devices. *Nat. Commun.* **14**, 2732 (2023).
- Yang, Y., et al. Anion-exchange membrane water electrolyzers and fuel cells. *Chem. Soc. Rev.* **51**, 9620–9693 (2022).
- Zuo, P. et al. Near-frictionless ion transport within triazine framework membranes. *Nature* **617**, 299–305 (2023).
- Salvatore, D. A. et al. Designing anion exchange membranes for CO₂ electrolyzers. *Nat. Energy* **6**, 339–348 (2021).
- Yang, Y. et al. Electrocatalysis in alkaline media and alkaline membrane-based energy technologies. *Chem. Rev.* **122**, 6117–6321 (2022).
- Kusoglu, A. & Weber, A. Z. New insights into perfluorinated sulfonic-acid ionomers. *Chem. Rev.* **117**, 987–1104 (2017).

13. Du, N. et al. Anion-exchange membrane water electrolyzers. *Chem. Rev.* **122**, 11830–11895 (2022).
14. Rykrkraglund, M. et al. Ion-solvating membranes as a new approach towards high rate alkaline electrolyzers. *Energy Environ. Sci.* **12**, 3313–3318 (2019).
15. Hu, X. et al. An operationally broadened alkaline water electrolyser enabled by highly stable poly(oxindole biphenylene) ion-solvating membranes. *Nat. Energy*, (2024).
16. Wu, X. Y., Chen, N. J., Klok, H. A., Lee, Y. M. & Hu, X. L. Branched Poly(Aryl Piperidinium) membranes for anion-exchange membrane fuel cells. *Angew. Chem. Int. Ed.* **61**, e202114892 (2022).
17. Marino, M. G., Melchior, J. P., Wohlfarth, A. & Kreuer, K. D. Hydroxide, halide and water transport in a model anion exchange membrane. *J. Membr. Sci.* **464**, 61–71 (2014).
18. Li, N. & Guiver, M. D. Ion transport by nanochannels in ion-containing aromatic copolymers. *Macromolecules* **47**, 2175–2198 (2014).
19. Campbell, M. G., Sheberla, D., Liu, S. F., Swager, T. M. & Dincă, M. Cu₃(hexaiminotriphenylene)₂: An electrically conductive 2D Metal–Organic Framework for chemiresistive sensing. *Angew. Chem. Int. Ed.* **54**, 4349–4352 (2015).
20. Wang, J. et al. Poly(aryl piperidinium) membranes and ionomers for hydroxide exchange membrane fuel cells. *Nat. Energy* **4**, 392–398 (2019).
21. Liu, J. et al. High-performance and scalable poly(terphenyl-furan piperidinium) membrane for anion exchange membrane fuel cell with 2 W cm⁻² of peak power density. *J. Membr. Sci.* **692**, 122260 (2024).
22. Zhang, F. et al. A π -conjugated anion-exchange membrane with an ordered ion-conducting channel via the McMurray coupling reaction. *Angew. Chem. Int. Ed.* **62**, e202215017 (2022).
23. Chen, N. et al. Insight into the alkaline stability of n-heterocyclic ammonium groups for anion-exchange polyelectrolytes. *Angew. Chem. Int. Ed.* **60**, 19272–19280 (2021).
24. Zhang, J., Luo, W. & Züttel, A. Crossover of liquid products from electrochemical CO₂ reduction through gas diffusion electrode and anion exchange membrane. *J. Catal.* **385**, 140–145 (2020).
25. Li, Y. C. et al. Bipolar membranes inhibit product crossover in CO₂ electrolysis cells. *Adv. Sustain. Syst.* **2**, 1700187 (2018).
26. Dubouis, N. et al. Tuning water reduction through controlled nanoconfinement within an organic liquid matrix. *Nat. Catal.* **3**, 656–663 (2020).
27. Tunuguntla, R. H., Allen, F. I., Kim, K., Belliveau, A. & Noy, A. Ultrafast proton transport in sub-1-nm diameter carbon nanotube porins. *Nat. Nanotechnol.* **11**, 639–644 (2016).
28. Zuo, P., Li, Y., Wang, A., Tan, R. & Xu, T. Sulfonated microporous polymer membranes with fast and selective ion transport for electrochemical energy conversion and storage. *Angew. Chem. Int. Ed.* (2020).
29. Zhu, Q. et al. A sulfonated ultramicroporous membrane with selective ion transport enables osmotic energy extraction from multiform salt solutions with exceptional efficiency. *Energy Environ. Sci.* **15**, 4148–4156 (2022).
30. Yang, C. et al. Copper-coordinated cellulose ion conductors for solid-state batteries. *Nature* **598**, 590–596 (2021).
31. Liu, M., Wang, S. & Jiang, L. Nature-inspired superwettability systems. *Nat. Rev. Mater.* **2**, 17036 (2017).
32. Yu, Z.-L. et al. Emerging bioinspired artificial woods. *Adv. Mater.* **33**, 2001086 (2021).
33. Zhang, C. et al. A synthetic Mn₄Ca-cluster mimicking the oxygen-evolving center of photosynthesis. *Science* **348**, 690–693 (2015).
34. Sun, L. C. A closer mimic of the oxygen evolution complex of photosystem II. *Science* **348**, 635–636 (2015).
35. Chang, B.-M. & Keller, M. Cuticle and skin cell walls have common and unique roles in grape berry splitting. *Hortic. Res.* **8**, 168 (2021).
36. Liu, S., Jobert, F., Rahnesan, Z., Doyle, S. M. & Robert, S. Solving the puzzle of shape regulation in plant epidermal pavement cells. *Annu. Rev. Plant Biol.* **72**, 525–550 (2021).
37. Liu, N., Karunakaran, C., Lahlali, R., Warkentin, T. & Bueckert, R. A. Genotypic and heat stress effects on leaf cuticles of field pea using ATR-FTIR spectroscopy. *Planta* **249**, 601–613 (2018).
38. Zhao, W. et al. of plant and fungal cell walls: A critical review. *Solid State Nucl. Magn. Reson.* **107**, 101660 (2020).
39. Phyto, P., Gu, Y. & Hong, M. Impact of acidic pH on plant cell wall polysaccharide structure and dynamics: insights into the mechanism of acid growth in plants from solid-state NMR. *Cellulose* **26**, 291–304 (2019).
40. Liu, N., Karunakaran, C., Lahlali, R., Warkentin, T. & Bueckert, R. A. Genotypic and heat stress effects on leaf cuticles of field pea using ATR-FTIR spectroscopy. *Planta* **249**, 601–613 (2019).
41. Demir, D., Ceylan, S., Göktürk, D. & Bölgen, N. Extraction of pectin from albedo of lemon peels for preparation of tissue engineering scaffolds. *Polym. Bull.* **78**, 2211–2226 (2021).
42. Stiefel, P., Schmidt-Emrich, S., Maniura-Weber, K. & Ren, Q. Critical aspects of using bacterial cell viability assays with the fluorophores SYTO9 and propidium iodide. *BMC Microbiol.* **15**, 36 (2015).
43. Cosgrove, D. J. Growth of the plant cell wall. *Nat. Rev. Mol. Cell Biol.* **6**, 850–861 (2005).
44. Li, F., Thevenon, A., Rosas-Hernández, A., Wang, Z. & Sargent, E. H. Molecular tuning of CO₂-to-ethylene conversion. *Nature* **577**, 509–514 (2020).
45. Wang, X. et al. Efficient electrosynthesis of n-propanol from carbon monoxide using a Ag–Ru–Cu catalyst. *Nat. Energy* **7**, 170–176 (2022).
46. Xu, Y. et al. Low coordination number copper catalysts for electrochemical CO₂ methanation in a membrane electrode assembly. *Nat. Commun.* **12**, 2932 (2021).
47. Yin, Z. et al. An alkaline polymer electrolyte CO₂ electrolyzer operated with pure water. *Energy Environ. Sci.* **12**, 2455–2462 (2019).
48. Ye, D. et al. Preferred crystallographic orientation of cellulose in plant primary cell walls. *Nat. Commun.* **11**, 4720 (2020).
49. Gilliam, R. J., Graydon, J. W., Kirk, D. W. & Thorpe, S. J. A review of specific conductivities of potassium hydroxide solutions for various concentrations and temperatures. *Int. J. Hydrog. Energy* **32**, 359–364 (2007).
50. Ceriotti, M. et al. Nuclear quantum effects in water and aqueous systems: experiment, theory, and current challenges. *Chem. Rev.* **116**, 7529–7550 (2016).
51. Agmon, N. The Grotthuss mechanism. *Chem. Phys. Lett.* **244**, 456–462 (1995).
52. Chen, M. et al. Hydroxide diffuses slower than hydronium in water because its solvated structure inhibits correlated proton transfer. *Nat. Chem.* **10**, 413–419 (2018).
53. Riccardi, D. et al. “Proton Holes” in long-range proton transfer reactions in solution and enzymes: a theoretical analysis. *J. Am. Chem. Soc.* **128**, 16302–16311 (2006).
54. Hu, J. et al. Layered double hydroxide membrane with high hydroxide conductivity and ion selectivity for energy storage device. *Nat. Commun.* **12**, 3409 (2021).
55. Sulpizi, M., Gaigeot, M.-P. & Sprik, M. The Silica–water interface: how the silanols determine the surface acidity and modulate the water properties. *J. Chem. Theory Comput.* **8**, 1037–1047 (2012).
56. Dereka, B. et al. Crossover from hydrogen to chemical bonding. *Science* **371**, 160–164 (2021).
57. Shi, B. et al. Short hydrogen-bond network confined on COF surfaces enables ultrahigh proton conductivity. *Nat. Commun.* **13**, 6666 (2022).
58. Kibria, M. G. et al. Electrochemical CO₂ reduction into chemical feedstocks: from mechanistic electrocatalysis models to system design. *Adv. Mater.* **31**, 1807166 (2019).

59. Timoshenko, J. et al. Steering the structure and selectivity of CO₂ electroreduction catalysts by potential pulses. *Nat. Catal.* **5**, 259–267 (2022).
60. Phillips, J. C., et al. Scalable molecular dynamics with NAMD. *J. Comput. Chem.* **26**, 1781–1802 (2005).
61. Guvench, O. et al. CHARMM additive all-atom force field for carbohydrate derivatives and its utility in polysaccharide and carbohydrate–protein modeling. *J. Chem. Theory Comput.* **7**, 3162–3180 (2011).
62. Vanommeslaeghe, K. et al. CHARMM general force field: A force field for drug-like molecules compatible with the CHARMM all-atom additive biological force fields. *J. Comput. Chem.* **31**, 671–690 (2010).
63. Ren, S. et al. Molecular electrocatalysts can mediate fast, selective CO₂ reduction in a flow cell. *Science* **365**, 367–369 (2019).
64. Yu, L. et al. Ultrafast room-temperature synthesis of porous S-doped Ni/Fe (oxy)hydroxide electrodes for oxygen evolution catalysis in seawater splitting. *Energy Environ. Sci.* **13**, 3439–3446 (2020).
65. Pang, J. et al. Synthesis of highly polymerized water-soluble cellulose acetate by the side reaction in carboxylate ionic liquid 1-ethyl-3-methylimidazolium Acetate. *Sci. Rep.* **6**, 33725 (2016).
66. Dai, Q. et al. Publisher Correction: Thin-film composite membrane breaking the trade-off between conductivity and selectivity for a flow battery. *Nat. Commun.* **11**, 2609 (2020).
67. Kim, Y. et al. Ionic highways from covalent assembly in highly conducting and stable anion exchange membrane fuel cells. *J. Am. Chem. Soc.* **141**, 18152–18159 (2019).
68. Darden, et al. Particle mesh Ewald: An N-log(N) method for Ewald sums in large systems. *J. Chem. Phys.* **98**, 10089–10092 (1993).

Acknowledgements

We acknowledge the National Key R&D Program of China (2022YFA0911900), the National Natural Science Foundation of China (22109128, 22088102), the Research Center for Industries of the Future (RCIF) at Westlake University for financial support of this work. We thank the Instrumentation and Service Center for Molecular Science and the Instrumentation and Service Center for Physical Sciences at Westlake University for assistance in measurement/data interpretation, and the Microscopy Core Facility of Westlake University for advice and assistance with electron and light microscopy sample preparation and data collection, Mr. Xin Cui for providing the preparation method for the anode catalyst and Prof. Xiaobo Li, Prof. Xin Zhang, and Prof. Ying Gu for fruitful discussions. We thank the Key Laboratory of Nuclear Solid State Physics Hubei Province (School of Physics and Technology, Wuhan University, Wuhan 430072, China) for providing technical support in PALS testing.

Author contributions

Qinglu Liu and Tang Tang contributed equally to this work in designing the presented experiments and carrying out the subsequent data

analysis. Ziyu Tian executed ¹H NMR analysis and prepared watermelon skin samples. Shiwen Ding and Lin Liu performed and analyzed the environmental scanning electron microscope image of watermelon skin. Linqin Wang performed the transmission electron microscope and scanning electron microscope imaging. Dexin Chen contributed to data mapping. Solid-state NMR Data analysis was performed by Xingyu Lu. GWAX Data analysis was performed by Xiaohe Miao. Zhiwei Wang, Wentao Zheng, and Husileng Lee participated in the construction of the CO₂RR experimental setup and performed the measurements. Licheng Sun contributed to the conceptualization, funding acquisition, resources, supervision, and manuscript review and editing. All authors contributed to the manuscript revision.

Competing interests

The authors declare no competing interests.

Additional information

Supplementary information The online version contains supplementary material available at <https://doi.org/10.1038/s41467-024-51139-6>.

Correspondence and requests for materials should be addressed to Licheng Sun.

Peer review information *Nature Communications* thanks Yu seung kim, Young Moo Lee and the other anonymous, reviewer(s) for their contribution to the peer review of this work. A peer review file is available.

Reprints and permissions information is available at <http://www.nature.com/reprints>

Publisher's note Springer Nature remains neutral with regard to jurisdictional claims in published maps and institutional affiliations.

Open Access This article is licensed under a Creative Commons Attribution-NonCommercial-NoDerivatives 4.0 International License, which permits any non-commercial use, sharing, distribution and reproduction in any medium or format, as long as you give appropriate credit to the original author(s) and the source, provide a link to the Creative Commons licence, and indicate if you modified the licensed material. You do not have permission under this licence to share adapted material derived from this article or parts of it. The images or other third party material in this article are included in the article's Creative Commons licence, unless indicated otherwise in a credit line to the material. If material is not included in the article's Creative Commons licence and your intended use is not permitted by statutory regulation or exceeds the permitted use, you will need to obtain permission directly from the copyright holder. To view a copy of this licence, visit <http://creativecommons.org/licenses/by-nc-nd/4.0/>.

© The Author(s) 2024